LANGMUIR

pubs.acs.org/Langmuir Article

Multilayer Langmuir Film of Monodisperse Au Nanoclusters: Unusual Growth via Bilayers

Simon Mičky, Michal Bodík, Maja Mičetić, Florian Fetzer, Markus Strienz, Vladimír Held, Matej Jergel, Andreas Schnepf, Frank Schreiber, and Peter Šiffalovič*

Cite This: *Langmuir* 2022, 38, 14850−14856 Read Online

ACCESS | Metrics & More | Article Recommendations | Supporting Information

ABSTRACT: The assembly of nanomaterials into thin films is an important area in the nanofabrication of novel devices. The monodispersity of nanoparticles plays an essential role in the resulting quality of the assembled mono- and multilayers. Larger polydispersity leads to smaller lateral correlation lengths and smaller domains of aligned nanoparticles, thus resulting in more point and line defects. Perfectly monodisperse nanoparticles should therefore minimize the number of defects in the assembled films. Despite tremendous progress in reducing the polydispersity of nanoparticles, there has been limited research on the assembly of thin films out of perfectly monodisperse nanoclusters. Here, we show a formation of Langmuir films using perfectly monodisperse gold nanoclusters with composition $Au_{32}(^{n}Bu_3P)_{12}Cl_8$ exhibiting a diameter of 1.8 nm. Using both *in situ* and *ex situ* small-angle X-ray scattering, we show that the monolayer formed on a Langmuir−Blodgett trough exhibits long-range order. Moreover, after compressing the monolayer, we found that the stress accumulated prior to the monolayer collapse triggers a transition to a short-range order not previously reported. If such monolayer is compressed further, the second layer is not formed as in the case of standard nanoparticles. Instead, a growth of islands by an odd number of layers is observed, leading to a thin film with a structure consisting of two different orientations of the hexagonal lattice. Such anomalous behavior may have implications for the possibilities of thin-film formation.

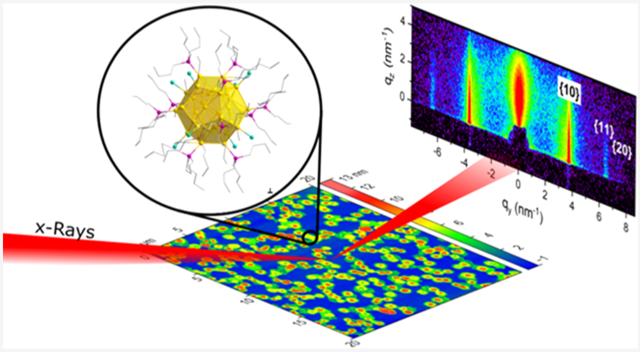

■ INTRODUCTION

The need for miniaturization requires developing novel approaches on how to build even smaller, yet functional devices. One of these approaches is by utilizing nanoparticles and incorporating them into devices.[1−5] Either individual nanoparticles can be utilized[6] or nanoparticles assembled into a thin layer.[7−10]

In order to prepare organized films of nanomaterials, self-assembly methods are commonly used.[11−16] Continuous films of nanoparticles are usually prepared from colloidal solutions by spin-coating,[17] dip-coating,[18] inkjet printing,[19] or Langmuir−Blodgett (LB) deposition.[20] Of these, the LB method allows the best control over the deposition process. By the lateral compression of the film by using movable barriers, the surface density of the material can be controlled very accurately. In theory, this should allow the formation of a film consisting of either a monolayer, or an arbitrary number of successive multilayers.

The formation of ordered structures has an influence on the resulting physical properties of the film.[21−24] However, one of the limiting factors for the formation of long-range order is the polydispersity of the used nanoparticles. A non-zero width of the nanoparticles' size distribution precludes the existence of long-range order in the assembled film.[25] By tuning the synthesis process, nanoparticles with a polydispersity below 10% can be synthetized.[26,27] The deposition of such virtually monodisperse nanoparticles results in films having a domain size of several micrometers squared.[28]

The deposition process of almost monodisperse nanoparticles can more easily result in high-quality films. Lambert et al.[29] observed a distinct phase transition in Langmuir films of CdSe quantum dots. In their work, the quantum dots were 4.0 nm in diameter with a standard deviation of only 0.28 nm. Using a LB trough, they monitored the surface pressure during the compression of such quantum dots. The isothermal compression resulted in distinct plateaus observed in the surface pressure. Analysis of LB films revealed that each plateau corresponds to the formation of a new layer, and the sharp

Received: September 13, 2022
Revised: November 8, 2022
Published: November 28, 2022

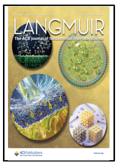

https://doi.org/10.1021/acs.langmuir.2c02514

increase in the surface pressure corresponds to the collapse of the fully formed layer.

Some attempts to investigate Langmuir films of monodisperse metalloid clusters have been published.[30,31] For instance, Swierczewski et al.[31] investigated Langmuir films of $Au_{38}(SC_2H_4Ph)_{24}$ clusters with purely hydrocarbon ligands. They were unable to demonstrate the formation of long-range crystalline order in the thin films of these nanoclusters, or the mode of the multilayer growth.

Recently, Kenzler et al.[32] produced the metalloid cluster compound $Au_{32}(^{n}Bu_3P)_{12}Cl_8$. These nanoclusters consist of a polyhedral core of gold atoms 0.9 nm in diameter surrounded by a ligand sphere with a total diameter of 1.8 nm (Figure 1).

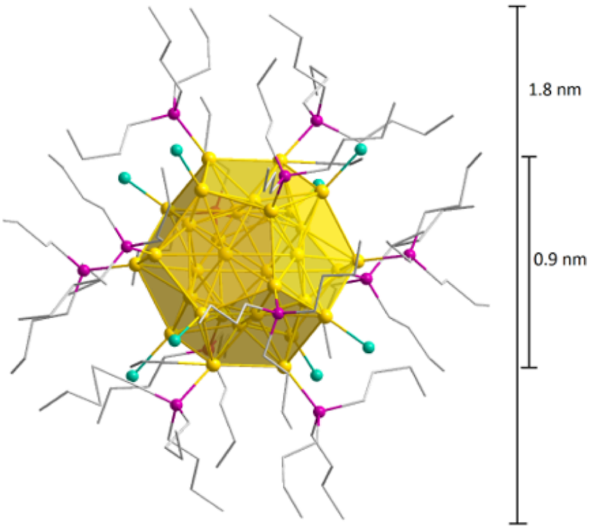

Figure 1. Molecular structure of the $Au_{32}(^{n}Bu_3P)_{12}Cl_8$ nanocluster in the solid state. All atoms except carbon are displayed as balls. Hydrogen atoms are omitted for clarity. Au: yellow, P: violet, Cl: green, and C: gray. The polyhedral arrangement of the gold atoms is highlighted.

They are atomically precise, and therefore truly monodisperse. By using these nanoclusters, monocrystals with a size of several hundred micrometers squared were prepared.[33] Such crystals exhibited additional optical transitions as well as an improvement of charge carrier transport by two orders of magnitude compared to polycrystalline films made from the same nanoclusters.

In this work, we prepared mono- and multi-layer Langmuir films of $Au_{32}(^{n}Bu_3P)_{12}Cl_8$ nanoclusters. The Langmuir monolayer exhibited long-range order that upon compression transformed into short-range order due to accumulated stresses. The atomic force microscopy (AFM) analysis showed that further film compression resulted in non-standard layer-by-layer growth. The surprising key finding is that the monolayer of gold nanoclusters does not form a double layer when compressed; instead, some triple-layered islands emerged. In addition, we analyzed the resulting films at different surface pressures and employed *ex situ* and *in situ* grazing-incidence small-angle X-ray scattering (GISAXS) in order to observe the formation of the film. GISAXS analysis revealed that the multilayer film consists of domains with two different orientations of a simple hexagonal lattice.

■ RESULTS

Surface Pressure−Area Isotherm. Figure 2 shows a typical surface pressure−area (Π−*A*) isotherm and compression modulus obtained during compression of gold nanoclusters on an LB trough. The figure displays a typical progression: gaseous phase → continuous monolayer → monolayer collapse. Region I indicates a gaseous phase, with no visible increase of Π with respect to area. As soon as a continuous coverage by the nanoclusters is reached, further compression results in a steep increase of the surface pressure and a distinct peak in the compression modulus (region II). As the compression continues, the collapse of the monolayer occurs as the nanoclusters are pushed from the first layer into the following layers. Since this process requires a relatively constant amount of energy per nanocluster, we get a level-off in the Π−*A* curve and a corresponding decrease in the compression modulus.

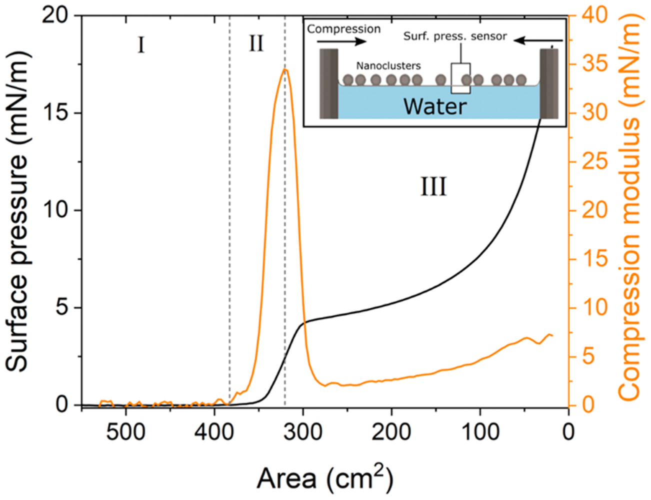

Figure 2. Typical Π−*A* isotherm (black) and compression modulus (orange) obtained during compression of the gold nanocluster film on an LB trough. The step indicates the formation and subsequent collapse of a well-ordered monolayer. Inset shows a diagram depicting the compression of the nanoclusters on the LB trough.

However, despite this, we did not obtain a completely level region followed by a second step, like in the case of the previously mentioned quantum dots.[29] A perfectly flat region would indicate that a constant energy per nanocluster is required to form the next layer, which occurs in the case of layer-by-layer growth. Since a perfectly flat region is not observed here, this implies that the next layers start to form before the previous layers have been completed.

GISAXS of Transferred Films. In order to gain insight into the internal structure of the nanocluster films, we measured GISAXS patterns of the assembled films transferred to Si substrates. Figure 3 shows *ex situ* GISAXS obtained from samples deposited at several different surface pressures. The first one, taken before the maximum in compression modulus (Π ≈ 1.5 mN/m), is shown in Figure 3a and the second one shortly after the maximum (Π ≈ 4 mN/m) in Figure 3b. The narrow truncation rods at lower Π (Figure 3a) suggest the presence of a monolayer exhibiting long-range order, while the expected hexagonal packing is confirmed by the presence of {11} and {20} diffractions at approximately 6.5 and 7.5 nm^{-1}, respectively. By analyzing the width of the truncation rods (see

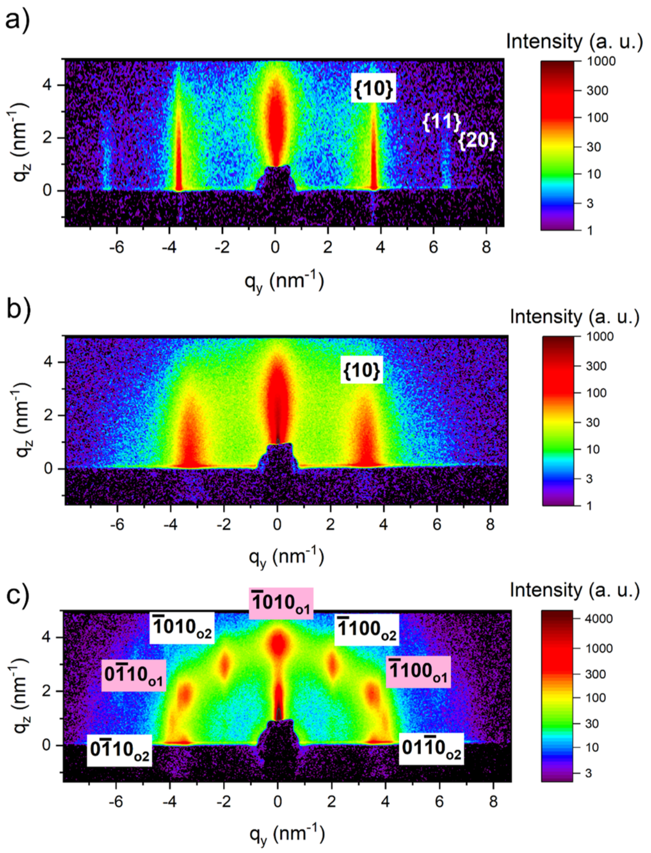

Figure 3. GISAXS maps of the gold nanocluster thin film at increasing stages of compression. (a) Before the closed monolayer (Π ≈ 1.5 mN/m), (b) after slight compression of the continuous monolayer (Π ≈ 4 mN/m), and (c) after further compression beyond the point of monolayer collapse (Π ≈ 10 mN/m). The diffractions in (c) are indexed by using Miller–Bravais indices.

the Supporting Information), we found that their width was on the instrumental limit, suggesting a substantial correlation length of the arrangement. From the peak positions, the center-to-center distance between the particles of 1.9 nm can be determined, which is in agreement with the previously determined diameter of these Au NCs.[33] In contrast to the state with low compression, a stark increase in the width of truncation rods when the maximum compression modulus is reached (Figure 3b) shows the accumulation of stresses in the film.[25] Larger peak width corresponds to a shorter correlation length (8.6 nm, equal to approximately 4.5 NCs), confirming that the high stress causes a loss of the long-range order within the arrangement not previously reported. Additionally, the disorder causes a shift in the position of the truncation rods from 3.7 to 3.3 nm^{-1}, which is expected after a drastic decrease of the correlation length.[25] Figure 3c shows a GISAXS map at Π ≈ 10 mN/m, which is beyond the monolayer collapse pressure. The phase transition to a multilayer film is apparent as multiple new peaks appear at $q_z > 0$ nm^{-1}. In order to understand what structure gives rise to such a diffraction pattern, we performed numerical simulations of the GISAXS maps.

Numerical Simulation of the GISAXS Patterns. The GISAXS maps were numerically simulated using a paracrystal model.[34,35] A simple hexagonal lattice with parameters $a = b$, c; $\alpha = 90°$, $\beta = 90°$, $\gamma = 120°$ was assumed, while the particles had a spherical form factor with radius R. The measured map and its simulation are given in Figure 4. Good agreement between the experiment and the simulation was obtained for a hexagonal lattice rotated in such a way that the base hexagons are placed perpendicularly to the substrate, as shown in Figure 4c. The number of spots present on the GISAXS patterns is larger than would be expected for a single orientation of a simple crystalline structure. For instance, a hexagonal lattice cannot produce more than four first-order diffractions in grazing-incidence geometry. Thus, we presumed the structure to be composed of two different orientations distributed within independent domains. Therefore, two independent orientations o_1 and o_2, shown in Figure 4c, were used with equal contribution. Other orientations are also present and contribute to the visible polycrystalline-like ring, but they are not taken into account in the simulation shown here. We have

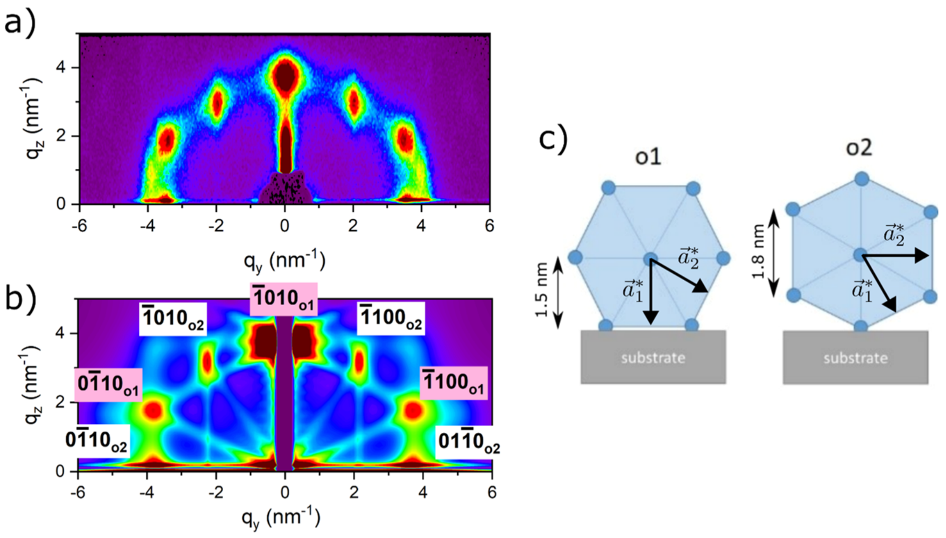

Figure 4. GISAXS maps of the (a) measured and (b) simulated intensity from a thin film of Au NCs. (c) Scheme of two different orientations of a simple hexagonal lattice used together in the simulation. The diffraction spots are indexed by using Miller–Bravais indices with the reciprocal space basis denoted in (c). The map in (a) is identical with the map in Figure 3c (Π ≈ 10 mN/m).

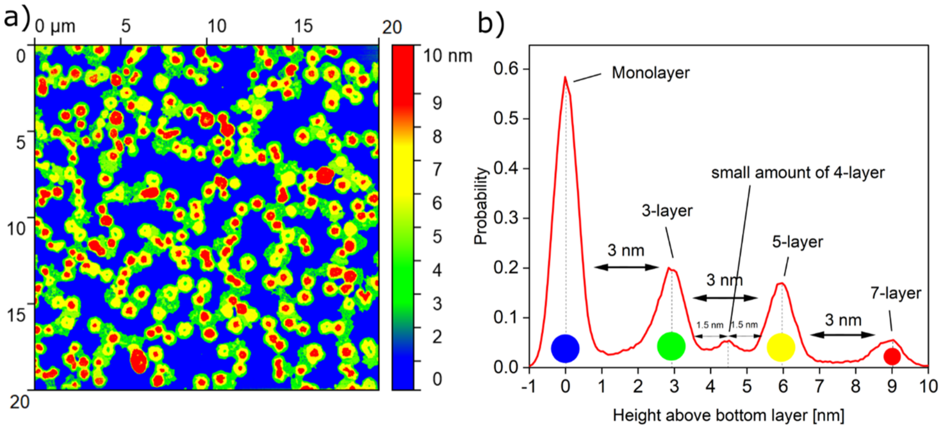

Figure 5. (a) AFM image of a film transferred at Π ≈ 10 mN/m. Each layer is indicated by a different color. (b) Corresponding height histogram. The differences of 3 nm suggest the terraces are made up of two layers of NCs.

assumed that the different orientations appear in domains that are randomly rotated around the normal to the surface.

The fitting process resulted in the following parameters: $a = b = 1.8 \pm 0.1$ nm, $c = 1.8 \pm 0.1$ nm, and $R = 0.48 \pm 0.05$ nm. The disorder of the NC position in the planes parallel and perpendicular to the films surface is $\sigma_{1-3}{}^{x,y} = 0.29 \pm 0.02$ nm and $\sigma_{1-3}{}^{z} = 0.09 \pm 0.02$ nm, respectively. The vertical separation between the layers of NCs that lie parallel to the substrate is 1.5 nm for the orientation o_1. For the orientation o_2, the top "layer" consists of lines alternating between heights of 1.8 and 0.9 nm. Therefore, the height measured by AFM is expected to lie somewhere between these two values, due to mechanical deformation of the layer by the AFM tip.

AFM of Transferred Films. To substantiate the measurements in reciprocal space, we performed surface topography measurements in real space using AFM. Scans of samples deposited at low Π confirm the presence of a flat layer covered by nucleation regions of growing multilayers (Figure S1). Figure 5 shows an AFM image together with the corresponding height histogram of a film deposited at post-collapse Π (10 mN/m).

The histogram indicates the presence of several well-defined layers with step heights of approximately 3 nm. The step height is quite similar to the longest edge of the unit cell of the single crystal of 3.32 nm. Referring to Figure 4c, this likely corresponds to the vertical separation between three layers of nanoclusters. This implies that the terraces do not grow as might be expected, that is, layer-by-layer. By presuming that material is conserved and calculating the expected amounts of NCs based on the coverage by each multilayer, we can deduce that the largest and bottommost area (with height of zero in the histogram, shown blue in the AFM image) corresponds to a monolayer of NCs. This means the AFM image is showing terraced Au NC islands growing on a monolayer. Together with the behavior of the Π−*A* isotherm, this demonstrates that the multilayer does not grow in the expected layer-by-layer manner. Rather a "layer-plus-island growth" (reminiscent of Stranski−Krastanov growth for epitaxial films) can be suggested as the actual growth mode.[36] Nevertheless, we do not intend to draw a direct analogy to Stranski−Krastanov growth, because the deposited material does not originate from the gas phase and condense on the solid surface, but is pushed up from the sides by the advancing barriers. The minor peak at 4.5 nm can be interpreted as a defect that violates the prevalent growth mode and can be identified as a small amount of monolayer lying on top of the three layers. More examples of AFM scans measured at different surface pressures which are consistent with the proposed growth via bilayers can be found in the Supporting Information (Figures S1−S3). The remarkable finding of growth via bilayers will be discussed below.

***In Situ* GISAXS.** To confirm that the observed behavior is not a result of transfer to substrates, we performed *in situ* GISAXS of the NC Langmuir film directly on the water surface. The GISAXS patterns were acquired continuously during the compression of the film. We found that the out-of-plane diffraction peaks appear only after compression beyond the point where a continuous monolayer is formed. Additionally, it is apparent that all out-of-plane peaks appear simultaneously and continuously (see Videos S1, S2, and S3). Figure S5 shows a combination of the Π−*A* isotherm, *in situ* GISAXS measurements, and multilayer coverage as deduced from *ex situ* AFM images.

■ DISCUSSION

The sharp and distinctive step-like Π−*A* isotherm is commonly observed for Langmuir films of small and highly monodisperse particles.[29] Our GISAXS investigations of Au nanocluster monolayers obtained at low surface pressures are in line with the results obtained via X-ray crystal structure analysis of the atomically precise metalloid cluster compound $Au_{32}(P^nBu_3)_{12}Cl$.[32] The width of the truncation rods limited by instrumental resolution confirms that the film consists of a hexagonally ordered monolayer exhibiting long-range order.

After compression to a critical Π, the perfect monolayer collapses. To the best of our knowledge, usually for Langmuir films, whether of 0D, 1D, or 2D nanomaterials, the compression to a critical Π results in a continuous formation of a double layer with an AB stacking.[37] However, in the case of the present monodisperse Au NCs, the second layer is formed by *two* nanoclusters simultaneously leaving the first monolayer and forming a three-layered structure. Consequently, the GISAXS patterns show an abrupt change in the scattering patterns. *In situ* GISAXS showed multiple new diffraction spots appearing simultaneously, thus validating the formation of a complex out-of-plane structure with a vertical correlation length beyond a simple bilayer. Thereafter, the position of the peaks does not change, only the total intensity gradually increases, and their width along q_z direction decreases, consistent with the growing number of layers.

https://doi.org/10.1021/acs.langmuir.2c02514
Langmuir 2022, 38, 14850−14856

AFM images show a terrace-like growth of NC islands instead of the second monolayer. Such behavior is unusual, because instead of an expected AB stacking of two hexagonal lattices, the film collapses into a crystalline structure with a non-trivial superlattice. To find the crystal structure corresponding to the GISAXS pattern obtained from the multilayer film, numerical simulations of the GISAXS patterns were performed. It was found that the pattern does not correspond to any simple stacking such as ABA or ABC. Instead, the film consists of domains with two different orientations of a hexagonal lattice. Additionally, both orientations are unusual in that the plane of hexagons is oriented perpendicularly to the surface instead of parallelly (Figure 4c).

AFM analysis showed that the height of such structure corresponds to approximately twice the size of an Au nanocluster. Further compression results in growth of the crystals by an even number of NC layers, while odd-numbered steps are very rarely observed. On top of that, uniaxial compression in a Langmuir trough typically results in a continuous uniaxial formation of the second layer, which is observed as stripes with substantial aspect ratios. However, here the Au nanoclusters formed crystals without any specific directionality. This is also unusual since it suggests that the formation of crystals is independent of the direction of compression.

Dai et al.[38] investigated the mechanism of monolayer collapse of several kinds of polydisperse nanoparticles ($d \sim 2$, 5.5, and 6 nm). They proposed "crinkle folding" and "S-folding" mechanisms, which could possibly lead to preferred growth from a monolayer directly to a tri-layer. However, these mechanisms also result in a specific orientation of the "crinkles", perpendicularly to the axis of compression, which is not observed here. Another mechanism for growth by an even number of layers was proposed by Ries and Swift for amphiphilic molecules.[39] This model of collapse of Langmuir films has been revisited by Goto and Caseli,[40] and their findings were that the mode of collapse is dependent on the functional groups present at the end of the molecules. Depending on the polarity and charge on each end of the amphiphilic molecule, the collapse of a monolayer can occur in different ways. In some cases, the ordering can be lost or the compression can lead to a formation of a triple layer immediately from a monolayer, as was also observed here. A possible explanation for our observation is thus that the growth of Au NC islands by two layers is caused by the anisotropic surface chemistry of the NCs. The tributylphosphine ligands are accompanied by atoms of chlorine, whose positions constitute the vertices of a cube (Figure 1). The relatively polar Au−Cl bond results in stronger mutual interactions than are present between the nonpolar butyls, where only the van der Waals forces are active. Since the distribution of Cl atoms on the surface is not uniform and the nanocluster is not spherically symmetric, this may lead to an anisotropic interaction which prefers multilayers with an odd-number of layers. On the other hand, the dipolar interaction between the chlorine ligands and water molecules could also help to stabilize the monolayer by lowering the tendency of the NCs to agglomerate. This surface chemistry can also be contrasted with the surface chemistry of $Au_{38}(SC_2H_4Ph)_{24}$ NCs previously used for Langmuir film formation,[31] which contain purely hydrophobic ligands.

■ CONCLUSIONS

In this work, we prepared Langmuir films of atomically precise and therefore truly monodisperse gold nanoclusters. Thanks to the monodispersity, a monolayer with long-range order was formed, exhibiting hexagonal packing. Prior to monolayer collapse, the accumulated stress led to a transition from long-range to short-range order. After further compression, the second layer was surprisingly not formed. Instead, the compression resulted in the formation of islands with an even number of layers on a pristine monolayer. Numerical simulations of the GISAXS maps revealed that the multilayer film consists of two different orientations of a hexagonal lattice. Furthermore, the *in situ* GISAXS confirmed that the multilayer islands are formed by bilayers rather than layer-by-layer growth.

Such anomalous behavior should not be energetically possible with standard isotropic interparticle interactions. This suggests that the atomically precise gold nanoclusters used in this work exhibit highly unusual surface chemistry.

■ EXPERIMENTAL SECTION

Materials. All chemicals were used as received. Ethanol-stabilized $CHCl_3$ was purchased from Sigma-Aldrich and Si/SiO_2 (native oxide) wafers were purchased from Si-Mat Silicon Materials.

Synthesis of $Au_{32}(^nBu_3P)_{12}Cl_8$ Nanoclusters. Nanoclusters were synthesized according to a previous publication.[32] $^nBu_3PAuCl$ was dissolved in ethanol (15 mL). Solid $NaBH_4$ (0.038 g, 1 mmol) dispersed in ethanol (15 mL) was added dropwise. The mixture was stirred for 1 h and the solvent was removed under reduced pressure. The remaining black solid was dissolved in CH_2Cl_2 (20 mL) and filtered out. The resulting solution was layered with 3 times of Et_2O. After 1 week, precipitation of elemental gold occurred, leaving a residual black supernatant. The supernatant was filtered and concentrated under vacuum. After several days at −30 °C, dark rectangular crystals of $Au_{32}(P^nBu_3)_{12}Cl_8$ formed. The characterization of the product was performed in the same publication[32] primarily by using single-crystal X-ray diffraction, which can happen exclusively in the case of monodisperse nanoparticles because a long-range order is a prerequisite for single-crystal growth.

Thin-Film Preparation. Thin films were prepared by using a modified Langmuir−Schaefer deposition method. The KSV Nima 1005 LB trough was first filled with ultrapure water subphase. The Si/SiO_2 substrates were placed on the bottom of the trough and tilted by supporting them with a washer. The nanoclusters dissolved in $CHCl_3$ were then deposited drop-by-drop onto the water surface by using a microsyringe. The submonolayer of nanoclusters was then compressed to the desired surface pressure, which was monitored by means of a Wilhelmy plate (inset of Figure 2). After the compression, the water surface was lowered by using a suction pump, depositing the film onto the substrates. The substrate tilt helped to achieve uniform deposition by causing a gradual sliding of the three-phase boundary. It was found that it is necessary to replace the supplied Teflon barriers on the LB trough with less hydrophobic barriers made of Delrin (polyoxymethylene), otherwise the water meniscus would not make a seal, and the material would leak past the barriers. The compression modulus was calculated from the surface pressure as $E = -\frac{d\Pi}{dA}A$.

Atomic Force Microscopy. Surface topography scans of the thin films on Si/SiO_2 substrates were made with Bruker Dimension Edge AFM in tapping mode with a scan size of 20 × 20 μm^2, scan speed of 0.5 Hz, and 512 × 512 points per scan. The AFM scans were processed by using the software Gwyddion.

Ex Situ Grazing-Incidence Small-Angle X-ray Scattering. Ex situ GISAXS measurements were performed on a Bruker Nanostar setup equipped with an Excillum MetalJet source and Pilatus 300K detector. The thin film on the Si/SiO_2 substrate was placed in the vacuum chamber and positioned by using a hexapod (Physik

Instrumente H-811). The source produced Ga Kα radiation (λ = 0.134 nm, E = 9.25 keV) and a beam size of 500 × 500 μm^2, with a photon flux of $\sim 10^{10}$ photons/s. The sample to detector distance was set to 233 mm, and the incidence angle used was 0.2°. The exposure time used was 10 min. The GISAXS maps were processed with the MATLAB toolbox GIXSGUI.

In Situ Grazing-Incidence Small-Angle X-ray Scattering. The in situ investigations were performed by directing the X-ray beam to the surface of the water perpendicularly to the long axis of the LB trough. The GISAXS maps were taken with an exposure time of 60 s throughout the whole duration of compression of the film. The IμS microfocus source (Incoatec) was placed on a heavy-load hexapod (Physik Instrumente H-840) to enable positioning of the X-ray beam. A Pilatus 200K detector was positioned 200 mm from the middle of the trough.

Numerical Simulations of the GISAXS Maps. The numerical analysis of the GISAXS maps was performed by using the software platform GisaxStudio.[41]

■ ASSOCIATED CONTENT

Supporting Information

The Supporting Information is available free of charge at https://pubs.acs.org/doi/10.1021/acs.langmuir.2c02514.

Calculation of the correlation length, more AFM topography images, and analysis of the *in situ* GISAXS (PDF)

Three examples of in situ GISAXS videos recorded during compression of the film on the LB trough (MP4, MP4, MP4)

■ AUTHOR INFORMATION

Corresponding Author

Peter Šiffalovič − *Institute of Physics, Slovak Academy of Sciences, 845 11 Bratislava, Slovakia; Center for Advanced Materials Application, 845 11 Bratislava, Slovakia;* orcid.org/0000-0002-9807-0810; Email: peter.siffalovic@savba.sk

Authors

Simon Mičky − *Institute of Physics, Slovak Academy of Sciences, 845 11 Bratislava, Slovakia;* orcid.org/0000-0001-8520-8887

Michal Bodík − *Nanotechnology Group, ETH Zürich, 8803 Rüschlikon, Switzerland*

Maja Mičetić − *Ruđer Boškovic Institute, 10000 Zagreb, Croatia;* orcid.org/0000-0002-5437-2972

Florian Fetzer − *Chemistry Department, University Tübingen, D-72076 Tübingen, Germany*

Markus Strienz − *Chemistry Department, University Tübingen, D-72076 Tübingen, Germany*

Vladimír Held − *Institute of Physics, Slovak Academy of Sciences, 845 11 Bratislava, Slovakia*

Matej Jergel − *Institute of Physics, Slovak Academy of Sciences, 845 11 Bratislava, Slovakia; Center for Advanced Materials Application, 845 11 Bratislava, Slovakia;* orcid.org/0000-0002-4482-7881

Andreas Schnepf − *Chemistry Department, University Tübingen, D-72076 Tübingen, Germany;* orcid.org/0000-0002-7719-7476

Frank Schreiber − *Institut für Angewandte Physik, Universität Tübingen, D-72076 Tübingen, Germany;* orcid.org/0000-0003-3659-6718

Complete contact information is available at: https://pubs.acs.org/10.1021/acs.langmuir.2c02514

Author Contributions

S.M. performed the film fabrication, measurements, analyzed the data, and interpreted the results. S.M. and M.B. wrote the manuscript. M.M. performed the GISAXS numerical simulations. F.F. and M.S. synthesized the nanoclusters. V.H. developed the thin-film deposition procedure. M.J., A.S., F.S., and P.S. conceived and supervised the project.

Notes

The authors declare no competing financial interest.

■ ACKNOWLEDGMENTS

We acknowledge the financial support of the projects DAAD, APVV-20-0111, APVV-19-0461, APVV SK-CN-RD-18-0006, APVV-17-0352, APVV-17-0560, APVV-15-0641, APVV-18-0480, APVV-19-0465, APVV-19-0365, APVV-14-0745, VEGA 2/0041/21, and VEGA 2/0046/21. This work was performed during the implementation of the project "*Building-up Centre for Advanced Materials Application of the Slovak Academy of Sciences*", ITMS project code 313021T081 supported by the Integrated Infrastructure Operational Programme funded by the ERDF.

■ REFERENCES

(1) Jheng, W. W.; Su, Y. S.; Hsieh, Y. L.; Lin, Y. J.; Tzeng, S. D.; Chang, C. W.; Song, J. M.; Kuo, W. Gold Nanoparticle Thin Film-Based Strain Sensors for Monitoring Human Pulse. *ACS Appl. Nano Mater.* **2021**, *4*, 1712−1718.

(2) Chen, H.; Zhou, Y.; Han, S. Recent Advances in Metal Nanoparticle-based Floating Gate Memory. *Nano Sel.* **2021**, *2*, 1245−1265.

(3) Jangjoy, A.; Bahador, H.; Heidarzadeh, H. A Comparative Study of a Novel Anti-Reflective Layer to Improve the Performance of a Thin-Film GaAs Solar Cell by Embedding Plasmonic Nanoparticles. *Plasmonics* **2021**, *16*, 395−401.

(4) Kagan, C. R.; Lifshitz, E.; Sargent, E. H.; Talapin, D. V. Building Devices from Colloidal Quantum Dots. *Science* **2016**, *353*, aac5523.

(5) Song, L.; Chen, J.; Xu, B. B.; Huang, Y. Flexible Plasmonic Biosensors for Healthcare Monitoring: Progress and Prospects. *ACS Nano* **2021**, *15*, 18822−18847.

(6) Wang, H.; Zhang, Z.; Su, M.; Sun, Y.; Mikhailova, J. V.; Cai, Z.; Wu, D.; Wang, K.; Pan, Q.; Chen, B.; Zuev, D.; Song, Y. A Coloration Biochip for Optical Virus Detection Based on Printed Single Nanoparticle Array. *Adv. Mater. Interfaces* **2022**, *9*, 2102164.

(7) Naqi, M.; Kwon, N.; Jung, S. H.; Pujar, P.; Cho, H. W.; Cho, Y. I.; Cho, H. K.; Lim, B.; Kim, S. High-Performance Non-Volatile in GaZnO Based Flash Memory Device Embedded with a Monolayer Au Nanoparticles. *Nanomaterials* **2021**, *11*, 1101.

(8) Liu, H.; Zeng, J.; Song, L.; Zhang, L.; Chen, Z.; Li, J.; Xiao, Z.; Su, F.; Huang, Y. Etched-Spiky Au@Ag Plasmonic-Superstructure Monolayer Films for Triple Amplification of Surface-Enhanced Raman Scattering Signals. *Nanoscale Horiz.* **2022**, *7*, 554−561.

(9) Lu, X.; Huang, Y.; Liu, B.; Zhang, L.; Song, L.; Zhang, J.; Zhang, A.; Chen, T. Light-Controlled Shrinkage of Large-Area Gold Nanoparticle Monolayer Film for Tunable SERS Activity. *Chem. Mater.* **2018**, *30*, 1989−1997.

(10) Song, L.; Qiu, N.; Huang, Y.; Cheng, Q.; Yang, Y.; Lin, H.; Su, F.; Chen, T. Macroscopic Orientational Gold Nanorods Monolayer Film with Excellent Photothermal Anticounterfeiting Performance. *Adv. Opt. Mater.* **2020**, *8*, 1902082.

(11) Murray, C. B.; Kagan, C. R.; Bawendi, M. G. Synthesis and Characterization of Monodisperse Nanocrystals and Close-Packed Nanocrystal Assemblies. *Annu. Rev. Mater. Sci.* **2000**, *30*, 545−610.

(12) Amadi, E. V.; Venkataraman, A.; Papadopoulos, C. Nanoscale Self-Assembly: Concepts, Applications and Challenges. *Nanotechnology* **2022**, *33*, 132001.

(13) Murray, C. B.; Kagan, C. R.; Bawendi, M. G. Self-Organization of CdSe Nanocrystallites into Three-Dimensional Quantum Dot Superlattices. *Science* **1995**, *270*, 1335−1338.

(14) Rawtani, D.; Agrawal, Y. K. Emerging Strategies and Applications of Layer-by-Layer Self-Assembly. *Nanobiomedicine* **2014**, *1*, 8.

(15) Albert, J. N. L.; Epps, T. H. Self-Assembly of Block Copolymer Thin Films. *Mater. Today* **2010**, *13*, 24−33.

(16) Song, L.; Xu, B. B.; Cheng, Q.; Wang, X.; Luo, X.; Chen, X.; Chen, T.; Huang, Y. Instant Interfacial Self-Assembly for Homogeneous Nanoparticle Monolayer Enabled Conformal "Lift-on" Thin Film Technology. *Sci. Adv.* **2021**, *7*, 2852.

(17) Hong, Y. K.; Kim, H.; Lee, G.; Kim, W.; Park, J. I.; Cheon, J.; Koo, J. Y. Controlled Two-Dimensional Distribution of Nanoparticles by Spin-Coating Method. *Appl. Phys. Lett.* **2002**, *80*, 844−846.

(18) Riau, A. K.; Mondal, D.; Setiawan, M.; Palaniappan, A.; Yam, G. H. F.; Liedberg, B.; Venkatraman, S. S.; Mehta, J. S. Functionalization of the Polymeric Surface with Bioceramic Nanoparticles via a Novel, Nonthermal Dip Coating Method. *ACS Appl. Mater. Interfaces* **2016**, *8*, 35565−35577.

(19) Chou, W. H.; Gamboa, A.; Morales, J. O. Inkjet Printing of Small Molecules, Biologics, and Nanoparticles. *Int. J. Pharm.* **2021**, *600*, 120462.

(20) Bodik, M.; Jergel, M.; Majkova, E.; Siffalovic, P. Langmuir Films of Low-Dimensional Nanomaterials. *Adv. Colloid Interface Sci.* **2020**, *283*, 102239.

(21) Sugi, K. S.; Maier, A.; Scheele, M. Emergent Properties in Supercrystals of Atomically Precise Nanoclusters and Colloidal Nanocrystals. *Chem. Commun.* **2022**, *58*, 6998−7017.

(22) Maiti, S.; Maiti, S.; Maier, A.; Hagenlocher, J.; Chumakov, A.; Schreiber, F.; Scheele, M. Understanding the Formation of Conductive Mesocrystalline Superlattices with Cubic PbS Nanocrystals at the Liquid/Air Interface. *J. Phys. Chem. C* **2019**, *123*, 1519−1526.

(23) Scheele, M.; Brütting, W.; Schreiber, F. Coupled Organic-Inorganic Nanostructures (COIN). *Phys. Chem. Chem. Phys.* **2015**, *17*, 97−111.

(24) Smilgies, D. M.; Hanrath, T. Superlattice Self-Assembly: Watching Nanocrystals in Action. *Europhys. Lett.* **2017**, *119*, 28003.

(25) Renaud, G.; Lazzari, R.; Leroy, F. Probing Surface and Interface Morphology with Grazing Incidence Small Angle X-Ray Scattering. *Surf. Sci. Rep.* **2009**, *64*, 255−380.

(26) Park, J.; Lee, E.; Hwang, N.-M.; Kang, M.; Kim, S. C.; Hwang, Y.; Park, J.-G.; Noh, H.-J.; Kim, J.-Y.; Park, J.-H.; Hyeon, T. One-Nanometer-Scale Size-Controlled Synthesis of Monodisperse Magnetic Iron Oxide Nanoparticles. *Angew. Chem.* **2005**, *117*, 2932−2937.

(27) Muzzio, M.; Li, J.; Yin, Z.; Delahunty, I. M.; Xie, J.; Sun, S. Monodisperse Nanoparticles for Catalysis and Nanomedicine. *Nanoscale* **2019**, *11*, 18946−18967.

(28) Wen, T.; Majetich, S. A. Ultra-Large-Area Self-Assembled Monolayers of Nanoparticles. *ACS Nano* **2011**, *5*, 8868−8876.

(29) Lambert, K.; Justo, Y.; Kamal, J. S.; Hens, Z. Phase Transitions in Quantum-Dot Langmuir Films. *Angew. Chem., Int. Ed.* **2011**, *50*, 12058−12061.

(30) Yokoyama, T.; Hirata, N.; Tsunoyama, H.; Negishi, Y.; Nakajima, A. Characterization of Floating-Gate Memory Device with Thiolate-Protected Gold and Gold-Palladium Nanoclusters. *AIP Adv.* **2018**, *8*, 065002.

(31) Swierczewski, M.; Maroni, P.; Chenneviere, A.; Dadras, M. M.; Lee, L. T.; Bürgi, T. Deposition of Extended Ordered Ultrathin Films of Au38(SC2H4Ph)24 Nanocluster Using Langmuir−Blodgett Technique. *Small* **2021**, *17*, 2005954.

(32) Kenzler, S.; Fetzer, F.; Schrenk, C.; Pollard, N.; Frojd, A. R.; Clayborne, A. Z.; Schnepf, A. Synthesis and Characterization of Three Multi-Shell Metalloid Gold Clusters Au 32 (R 3 P) 12 Cl 8. *Angew. Chem., Int. Ed.* **2019**, *58*, 5902−5905.

(33) Fetzer, F.; Maier, A.; Hodas, M.; Geladari, O.; Braun, K.; Meixner, A. J.; Schreiber, F.; Schnepf, A.; Scheele, M. Structural Order Enhances Charge Carrier Transport in Self-Assembled Au-Nanoclusters. *Nat. Commun.* **2020**, *11*, 1−8.

(34) Buljan, M.; Radić, N.; Bernstorff, S.; Dražić, G.; Bogdanović-Radović, I.; Holý, V. Grazing-Incidence Small-Angle X-Ray Scattering: Application to the Study of Quantum Dot Lattices. *Acta Crystallogr., Sect. A: Found. Crystallogr.* **2012**, *68*, 124−138.

(35) Basioli, L.; Salamon, K.; Tkalčević, M.; Mekterović, I.; Bernstorff, S.; Mičetić, M. Application of GISAXS in the Investigation of Three-Dimensional Lattices of Nanostructures. *Crystals* **2019**, *9*, 479.

(36) Lüth, H.*Solid Surfaces, Interfaces and Thin Films*; Graduate Texts in Physics; Springer International Publishing: Cham, 2015.

(37) Vegso, K.; Siffalovic, P.; Majkova, E.; Jergel, M.; Benkovicova, M.; Kocsis, T.; Weis, M.; Luby, S.; Nygård, K.; Konovalov, O. Nonequilibrium Phases of Nanoparticle Langmuir Films. *Langmuir* **2012**, *28*, 10409−10414.

(38) Dai, Y.; Lin, B.; Meron, M.; Kim, K.; Leahy, B.; Witten, T. A.; Shpyrko, O. G. Synchrotron X-Ray Studies of Rapidly Evolving Morphology of Self-Assembled Nanoparticle Films under Lateral Compression. *Langmuir* **2013**, *29*, 14050−14056.

(39) Ries, H. E.; Swift, H. Twisted Double-Layer Ribbons and the Mechanism for Monolayer Collapse. *Langmuir* **1987**, *3*, 853−855.

(40) Goto, T. E.; Caseli, L. Understanding the Collapse Mechanism in Langmuir Monolayers through Polarization Modulation-Infrared Reflection Absorption Spectroscopy. *Langmuir* **2013**, *29*, 9063−9071.

(41) GisaxStudio-modular, multi-platform program for GISAXS analysis. http://homer.zpr.fer.hr/gisaxstudio/doku.php. Accessed November 21, 2022.